Negative-index imaging by an index-matched photonic crystal slab

E. Schonbrun,[1] T. Yamashita,[2] W. Park,[1,*] and C. J. Summers[2]

[1]*Department of Electrical Engineering, University of Colorado at Boulder, Boulder, Colorado 80309, USA*
[2]*School of Materials Science and Engineering, Georgia Institute of Technology, Atlanta, Georgia 30332, USA*

We report negative-index imaging at near infrared wavelengths using a photonic crystal (PC) with an effective index matched closely to air as the incident medium. A tapered waveguide is used to generate a point-sourcelike object field; and to probe the focusing behavior of the PC, an array of 500 nm wide photonic wire waveguides is placed in the backplane of the PC lens. This represents a sampling of the image field at the rate of one data point per free space wavelength (λ_0). For TM polarization, a well-defined $1.7\lambda_0$ spot is observed, while the TE polarization lies near the photonic band edge and exhibits spreading and low transmission. We also investigate the wavelength dependence and experimentally show the performance of the negative index lens as a function of frequency.

I. INTRODUCTION

A slab of negative-index material (NIM) is capable of imaging incident electromagnetic fields by a mechanism that is much different than a normal lens. Propagation through a negative-index material phase conjugates the spatially dependent term of the wave. Due to the backward evolution of the phase fronts, NIMs generate an image of the incident field for a balanced length of propagation through positive and negative index materials.[1,2] Materials can achieve a negative effective phase index when certain resonant conditions are met inside the medium. Generally there are two different paths to achieving the kind of strong light-matter interaction needed for a negative phase velocity. One is to exploit naturally occurring properties of materials such as plasmonic[4] or polaritonic[5] resonance, and the other is to engineer material properties by fabricating wavelength scale periodic structures [photonic crystals (PCs)][6,7] or assemblies of much smaller resonant structures called metamaterials.[8] Of the latter, the first systems studied were composed of arrays of metal wires and split ring resonators designed to have simultaneous negative permittivity and permeability. These mediums are statically tunable in that the geometry of the structure can be designed to place the electromagnetic resonance at desired frequencies. However, they become lossy at optical frequencies due to the inherent imaginary part of the metal's permittivity. When used in near field configurations, imaging applications do not require a bulk, propagating mode, so only a negative permittivity is needed. Plasmonic resonance of metals and also polaritonic resonance of semiconductors have been used successfully to obtain negative permittivity. These single negative materials are, however, incapable of far field applications because no continuous or bulk mode can be excited in the media. This means that they must be operated in the near field and their thickness must be kept small.

In contrast to the limitation of having to work near a material resonance, PCs support waves with negative phase velocity whenever a photonic band with negative slope is excited. Also, the Bloch modes extend infinitely over the crystal dimensions, so backward wave propagation is not limited to thin structures. Recent studies have confirmed that Bloch waves couple efficiently to a large spatial spectrum of incident plane waves[9] as long as the interface is correctly chosen. These features make PCs an ideal medium for far field applications of NIMs including lens design,[10] polarization optical elements,[11] and open cavities.[12,13] Furthermore, PCs are in general purely dielectric systems with low intrinsic material loss, which is a clear advantage for optical frequency operation. As long as the mode that is excited lies underneath the cladding light cone, the loss in slab PC geometries arises solely from surface and sidewall roughness. Experimental demonstrations of light propagation through $10–50\lambda_0$ sized PC networks have shown their capability of low loss operation and control of light as a function of polarization, incidence angle, and frequency.[14–17]

Negative-index imaging by an InP-InGaAsP-InP PC slab in the near-infrared region has recently been reported.[3] While this work showed imaging due to negative refraction, it did not probe the field profile directly at the exit plane of the PC and did not discuss the index matching issue. In this paper, we present a silicon (Si)-based negative index PC structure that is index matched to air and images incident light after propagation through an equal length of negative and positive index mediums. We choose air as the incident medium instead of a silicon slab because it is not possible to match the negative effective index to the large value of silicon. We have previously reported negative refraction of a plane wave in a Si-polymer based PC structure index matched to air.[17] Here, we report a Si-air PC structure that images TM-polarized light and spatially disperses TE-polarized light. In this paper TM polarization is defined as the mode that has its magnetic field perpendicular to the direction of the waveguide and the symmetry axis of the PC, and the same is true for the electric field for the TE mode. The PC is located in an integrated device structure with clearly defined object and image planes. The object plane is defined by a specially designed waveguide tip and the image plane is located at a symmetric position on the backside of the PC where the transmitted light is sampled by an array of photonic wire waveguides.
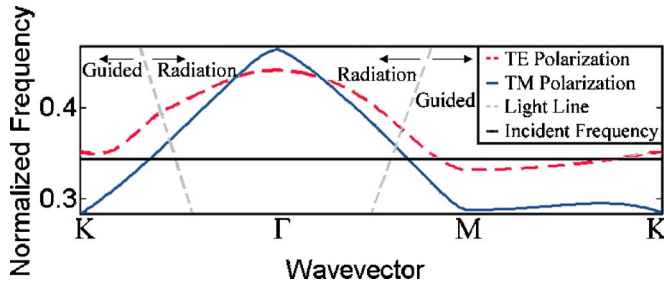
195117-1

FIG. 1. (Color online) TE and TM photonic band structure for the second band of a triangular lattice of air holes in silicon with a hole radius of 170 nm and a lattice constant of 540 nm. The bands are calculated using the finite element method. The thickness of the silicon layer is taken into account by using effective indices of $n_{eff}=2.53$ and $n_{eff}=3.02$ for the TM and TE polarizations, respectively. These values were obtained from the fundamental guided mode of 1550 nm light propagating in a 300 nm thick silicon ($n_{bulk}=3.45$) slab waveguide.

II. PHOTONIC CRYSTAL NEGATIVE INDEX

In general, the second photonic band of a planar PC exhibits negative slope due to the formation of Brillouin zones and consequent band folding. In this band, the modal frequency decreases as the magnitude of the momentum increases. If only the second band exists in a given frequency range, the phase of the excited wave progresses backwards and the momentum vector $\mathbf{k}$, and the fields $\mathbf{E}$ and $\mathbf{H}$ form a left-handed set. Near the top of the second band close to the Γ point, the equi-frequency surface (EFS) is circular,[12] so light behaves isotropically. In this case, $\mathbf{k}$ is antiparallel to the Poynting vector $\mathbf{S}$ at all angles, giving the medium a meaningful effective index less than zero. At the Γ point, the phase velocity is infinite. As the frequency is decreased from the top of the band, the magnitude of the effective index becomes larger and more anisotropic. In the case of a triangular lattice of holes described in the Fig. 1 caption, the effective index of TM polarization stays nearly isotropic until the second band intersects the air light line, which occurs at a normalized frequency ω_n ($\omega a/2\pi c$) of $\omega_n=0.35$ in our structure. This indicates a phase index of -1 and defines a phase velocity matching condition between the PC and air. For a negative index PC lens, this is the ideal operational frequency range.

The direction of energy propagation is along the gradient of the EFS. As shown in Fig. 2, we have designed the PC so that the TM polarization sees a concave dispersion surface and the TE polarization sees a convex dispersion surface. Effectively, this means that the PC spatially collects TM polarized light while spatially dispersing TE polarized light. In general, the high frequency region of the second photonic band is concave and the lower frequency region is convex with respect to the Γ point. By equating the second derivative of the band structure to zero, a spectral inflection point is defined where the curvature changes sign. This occurs at $\omega_n=0.327$ for TM light and at $\omega_n=0.369$ for TE light. Consequently, because our operating frequency of $\omega_n=0.345$ lies between these values we expect oppositely signed refraction for TE and TM polarizations. The refraction angle is deter-
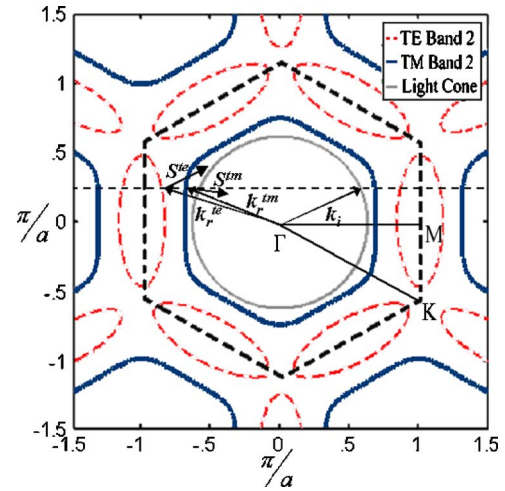

FIG. 2. (Color online) EFS curves for TE, TM, and air for $\omega_n=0.345$. Arrows and the dashed line illustrate the tangential momentum matching condition that occurs at the interface between air and the PC. $\mathbf{k}_i$ is the incident momentum, $\mathbf{k}_r$ is the refracted momentum for TE and TM, and $\mathbf{S}$ is the refracted Poynting vector for TE and TM. The TM EFS curve is concave and exhibits negative refraction, whereas the TE EFS curve is convex and exhibits positive refraction. While the TM EFS curve is not perfectly circular, the operating frequency is chosen so that the phase index is closely matched to that of air and has a modulus of slightly greater than 1 to ensure in-plane guiding.

mined by the Poynting vector $\mathbf{S}$ and can be positive or negative in the second band whereas the phase velocity is always negative.

III. INTEGRATED DEVICE DESIGN

A 10 μm wide Si ridge waveguide is fabricated with a tapered tip to generate a pointlike source, which terminates at $\lambda_0/2$ from the leading edge of the PC, where λ_0 is the central source wavelength of 1550 nm. The multimode ridge waveguide is tapered to a width of 920 nm corresponding to $3\lambda_0/2n_{eff}$ using the n_{eff} of the fundamental TM mode for a 300 nm thick silicon slab. Since it holds an integer number of half wavelengths, a $3\lambda_0/2n_{eff}$ wide aperture exhibits high transmission and also has a bright central radiation lobe that is similar to a point source.

The air gap between the waveguide tip and the PC has two important functions. First, it filters out large spatial frequencies that are evanescent in air. Even if the incident frequency only intersects a single photonic band in the first Brillouin zone, incident waves with large transverse $\mathbf{k}$ vectors may excite multiple Bloch waves in the crystal that arise from the intersection with higher order Brillouin zones.[18] These diffracted waves will not have antiparallel $\mathbf{k}$ and $\mathbf{S}$ vectors and consequently do not have desirable negative index properties because they do not originate from the same Γ point. The air gap filters all spatial frequencies that are large enough to generate diffracted waves. The second important feature of the air gap is that it allows the PC negative effective index to have the same modulus as the surrounding medium. When this occurs, the spatial frequency spectrum sup-
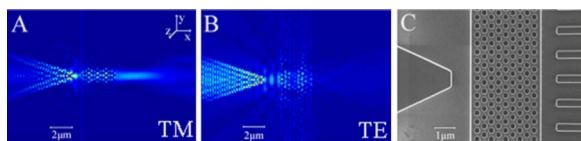
FIG. 3. (Color online) two-dimensional (2D) FDTD simulation of the time-averaged field modulus for (a) TM polarization (E_z) and (b) TE polarization (H_z). (c) Scanning electron micrograph of the fabricated device. The dimensions of the modeled structure are the same as the device shown in (c), though shown in a different scale. The simulation in (a) shows efficient negative index imaging of TM polarized light, where the FWHM of the image intensity has a width of $0.78\lambda_0$. The TE wave shown in (b) spreads as it propagates through the PC and suffers from higher reflection as shown by the depth of the modulation of the forward and backward waves in front of the PC.
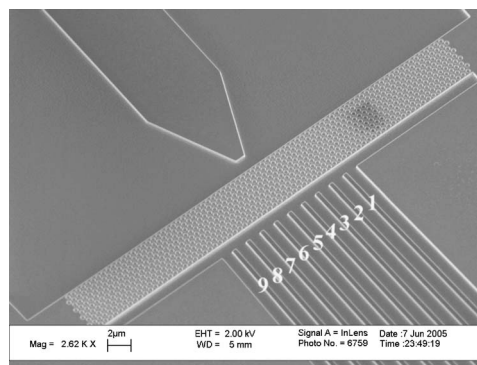

FIG. 4. Scanning electron microscopy (SEM) micrograph of a fabricated device tilted at a 30 deg angle showing smooth, anisotropic sidewalls. Regions surrounding the input tapered waveguide and the output photonic wires have been etched down to the bottom oxide layer so that the two PC interfaces are with air instead of the silicon slab. The nine output photonic wires are numbered and are used in Fig. 6.

ported by the two media is the same. This means that every incident tangential **k** vector is matched across the boundary and therefore there will be no total internal reflection (TIR). While for a flat lens geometry this occurs whenever the background medium has a lower effective index than the PC, for geometries without parallel interfaces a matched effective index is needed to avoid TIR at an internal interface. Another benefit of index matching is that the refracted angle in the PC always equals the incident angle. If the EFS curve is exactly circular, there will not be any spherical aberration when the index matching condition is satisfied. Furthermore, because there is no optical axis in a flat lens, all off axis aberrations will also be absent.

The finite-difference time-domain (FDTD) simulations in Figs. 3(a) and 3(b) show that this tip geometry produces an internal focus inside the taper with a full width at half maximum (FWHM) of $\lambda_0/5.9$ which is close to $\lambda_0/2n_{eff}$ for the TM light. The light expands to a spot with a FWHM of $\lambda_0/3.8$ in air at the end facet of the waveguide. The optical field then propagates in air to the interface of the PC, which consists of a triangular lattice of air holes with the surface normal oriented in the ΓM direction of the PC. The light couples into the second photonic band with an estimated efficiency of 75%, which was calculated by a modal field overlap method. In the current slab PC geometry, however, this value will be modified by the Fabry-Pérot resonance and also by the out-of-plane scattering. In any case, we note that the PC is not expected to exhibit 100% transmission even when the index is perfectly matched. The excited Bloch modes then negatively refract to the back interface of the PC and couple back out to plane waves in air. For TM polarized light, a well-defined image of the waveguide tip source is produced at a symmetric distance from the second PC interface and is subsequently sampled by an array of 500 nm wide photonic wire waveguides spaced by 1 μm as shown in Fig. 4. For TE polarized light, FDTD shows that the transmission is much lower and the PC region exhibits higher energy density because the excitation is close to the band edge. The photonic wires are 500 μm long and are fanned out at a small angle so that at the output they are spaced by 5 μm, and easily resolvable by an optical microscope. The use of a small fanning angle and the fact that the guides are spaced by twice their width prevents light from coupling into neighboring photonic wires, while still sampling the image at the rate of one data point per λ_0.

The device was fabricated utilizing electron beam lithography and inductively coupled plasma etching. The substrate was a silicon-on-insulator (SOI) wafer with 300 nm and 1 μm device and bottom oxide layer thickness, respectively. After etching, the remaining electron beam resist was cleaned utilizing an oxygen plasma followed by cleaving along the $\langle 100 \rangle$ plane of the wafer to create a smooth input facet.

IV. OPTICAL CHARACTERIZATION

The characterization consists of two parts. First, out-of-plane scattered light is collected and imaged over the waveguide tip and PC. The scattered light gives information on light propagation out of the device plane and is effectively complemented by the 2D FDTD simulations, which give information only about light in the device plane. The second part of the experimental procedure is to image the output of the fanned photonic wires that sample the image formed by the PC. This monitors light that has propagated through the entire device without being scattered out of plane. Because we are interested in optical modes near the air light line, there is some concern that the wave will be too loosely guided in the slab plane and will be subsequently lost. Thus, it is important to test the confinement of the light within the slab region, as well as to sample the imaged field. More detailed description on the experimental setup can be found in Ref. 17.

Figure 5 shows infrared photographs of the front and backplanes of the PC lens, and the outputs of the fanned-out photonic wires in the insets. The operating wavelength is 1562 nm. For both TM and TE polarizations, we observe a bright spot at the tip of the input waveguide, confirming the formation of a tightly focused and diverging incident field as
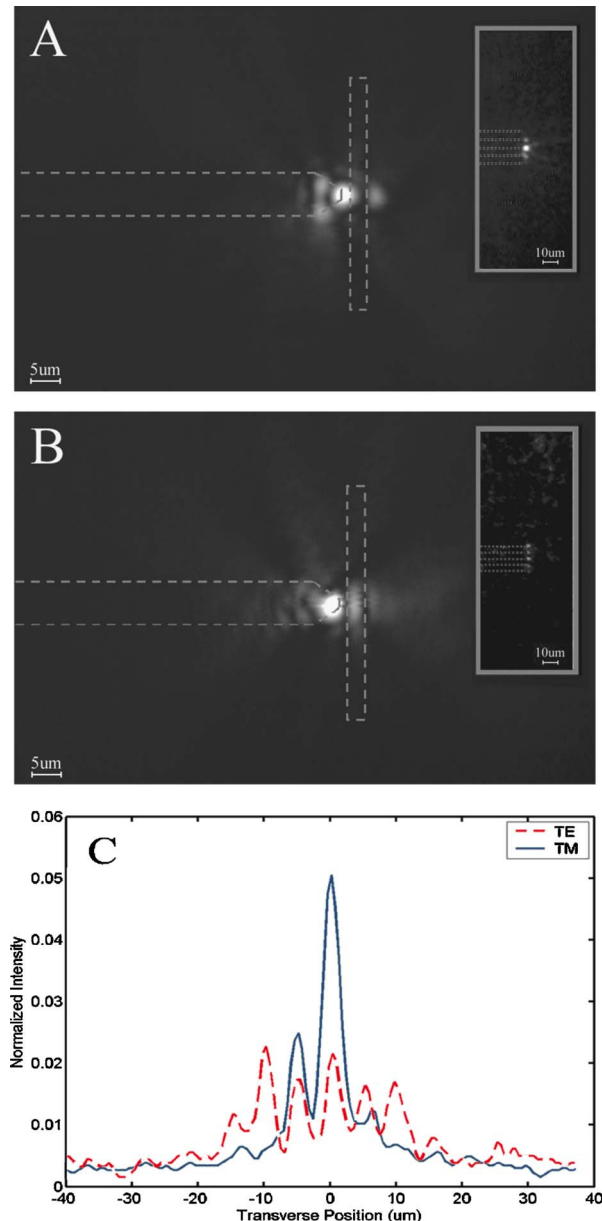
FIG. 5. (Color online) Experimental characterization of the device at an incident wavelength of 1562 nm (a) for TM and (b) for TE. The main panels show light collected over the waveguide tip and PC, and the insets show the output from the photonic wire array. Dotted lines have been imposed on the scattering data to help the reader visualize the device. The gain of the camera is higher in the insets than in the main pictures due to loss in the photonic wires, and the gain for TE is higher than TM due to the lower transmission of TE light. (c) The cross-sectional intensity is plotted at 1562 nm for both polarizations. The intensity is normalized to the integrated value of the cross section, eliminating the effect of the variable gain.

predicted in Fig. 3. It is clear from Fig. 5(a) that another bright spot is formed on the backplane of the PC lens for TM polarization. This demonstrates that the PC focuses the TM light with high efficiency. In contrast, we do not observe any well-defined bright spot for TE polarization. Instead, the light spreads significantly as shown in Fig. 5(b). Another feature of the FDTD simulation that is evident in the experiment is the relatively large transmission efficiency of the TM light compared to the large reflection of the TE wave at the interface, as shown by the more intense backscattering in Fig. 5(b). In the TE case, the PC region in Fig. 5(b) exhibits large out-of-plane scattering compared to the TM case in Fig. 5(a), which stays relatively dark.

The inset shows that the TM polarization primarily illuminates only a single photonic wire and that this mode is confined strongly enough to permit high transmission for the entire device. In contrast, the TE polarization illuminates five photonic wires almost evenly. Furthermore, the TE polarization has considerably less transmission and therefore we had to increase the integration time of the camera to obtain the infrared photographs in Figs. 5 and 6. The cross-sectional intensity at the output of the photonic wires plotted in Fig. 5(c) quantitatively shows the intensity distribution at the image plane. We verified that the response of the vidicon camera was linear by mapping the brightness of a pixel to the laser power. The average intensity of the first photonic wire above and below the central one is 37%. If the distribution were to be fit with a Gaussian line shape, the FWHM would be $1.7\lambda_0$. This value is approximately twice the width, $0.78\lambda_0$, obtained by FDTD simulation. However, we note that this should be interpreted as the upper bound of the spot size because we used a relatively coarse spatial sampling at intervals of $1\lambda_0$. In order to resolve features close to λ_0 and smaller, near-field techniques will be required. While it is possible that imperfect fabrication may have caused some broadening of the imaged spot, we emphasize that light is clearly being imaged onto the wire array and the central wire contains 58% of the total intensity in the array. In contrast, the TE light illuminates five photonic wires with a FWHM of approximately $5\lambda_0$. The central guide for TE contains only 19% of the intensity of the array. Since the width is significantly greater than our sampling rate in this case, the experimentally observed profile agrees well with the FDTD simulation.

V. SPECTRAL RESPONSE

To further substantiate our observation at 1562 nm, the wavelength dependence is investigated. As the second TM band crosses the air light line, the slope stays remarkably constant, as shown in Fig. 1. We therefore expect negative refraction with small group velocity dispersion in this region, and consequently the direction of S will change slowly with frequency. Figures 6(a) and 6(b) show infrared photographs of the output of the photonic wire array as a function of wavelength. For TM polarization, the PC images light to a spot size of the order of $2\lambda_0$ for the entire bandwidth of the C-band and L-band lasers from 1525 to 1605 nm. The peak transmission of the central waveguide occurs at 1562 nm, which is the best operating wavelength for this PC lens and occurs at the peak of Fabry-Pérot resonance between the front and back interfaces of the PC. From FDTD analysis, we found that the free spectral range in our frequency region for the PC is $\Delta\omega_n = 0.023$, which is slightly larger than the
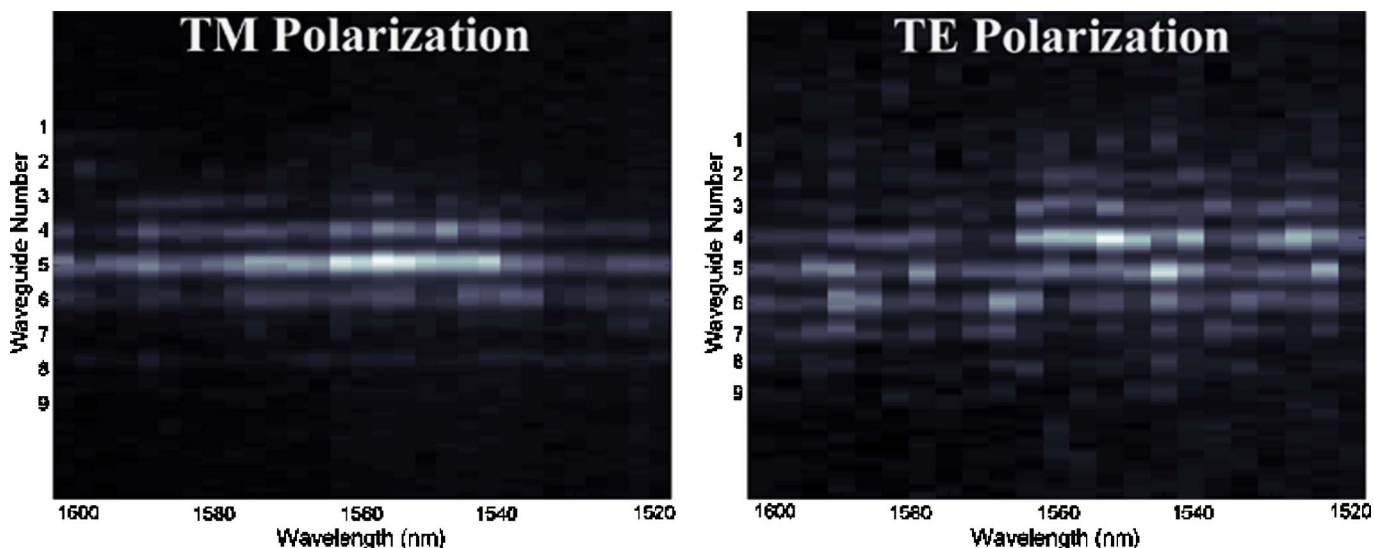
FIG. 6. (Color online) Wavelength dependence of photonic wire array's output. The wavelength is swept through the 80 nm bandwidth of a *C*-band and an *L*-band tunable laser for TM and TE, respectively. At each wavelength, an infrared camera captures the output of the photonic wires. TE data is recorded at a higher camera gain.

tuning bandwidth of our lasers. In scanning away from this peak, Fig. 6(a) shows a clear decrease in transmission, due to the increased reflection at the air-PC interface and the fact that the photonic wire array is no longer situated at the plane of best focus. At shorter wavelengths, higher out-of-plane scattering is expected because the excited mode lies outside the air light line and is no longer guided within the PC device plane. This effect should further decrease the transmission through the PC lens. At longer wavelengths, there is less out-of-plane scattering because the modes remain within the air light line. However, the imaging behavior degrades with increasing operating wavelength because the EFS curve becomes more hexagonally shaped and the PC approaches the self-collimation regime. Although our experimentally achievable tuning range does not reach the self-collimation regime, which is centered at the inflection point of the band structure in Fig. 1 (1651 nm in our structure), the deformation in the EFS curve deteriorates negative index imaging properties.

For TE polarized light, the output is spread over 5–7 waveguides throughout the wavelength range investigated. Also, the transmission is considerably lower than in the TM case. The second TE band has a smaller but more rapidly changing slope in this frequency region and thus the output of the device is much more sensitive to the wavelength. The smaller slope also decreases the free spectral range of the Fabry-Pérot oscillations to a value of $\Delta \omega_n = 0.016$ with the peak position at 1548 nm. On the long-wavelength side of the tuning range, we approach the band gap, which begins at 1660 nm. In this range, the EFS curve shrinks and thus the range of tangential $\boldsymbol{k}$ vectors that can couple into the PC decreases. This consequently causes higher reflection at the air-PC interface and the transmission decreases as shown in Fig. 6(b). In the short wavelength side of the spectrum, the transmission increases slightly. There are two reasons for this. First, the EFS curve expands in k space and thus more

incident k components are coupled into the PC. Also, we are working close to the self-collimation regime, which occurs at the inflection point at 1463 nm. Therefore, the EFS curve becomes flatter and the PC does not spatially disperse light as effectively as at longer wavelengths. If the self-collimation wavelength were obtainable with our laser, the output beam would have narrowed to an illumination of three photonic wires, similar to the long wavelength region of the TM spectrum. However, when scanning to shorter wavelengths, the PC exits the guiding regime and the excited mode lies outside the air light line, as was the case for TM polarization. Therefore, the out-of-plane loss is higher and this effect limits the increase in transmission.

VI. CONCLUSIONS

In summary, we have designed and fabricated photonic crystal structures that exhibit and give physical insight to negative index of refraction and index matching with air as the incident medium. The structure was designed to exhibit a negative index matched to air for TM polarization and contrasting dispersive behavior for TE polarization. Our experiments conducted in the near infrared frequency region clearly showed the intended behaviors for both polarizations. We also investigated the frequency dependence of the imaging behavior and discussed the issue of index matching and its impact on negative-index PC lens performance. The number of degrees of freedom in the photonic crystal approach, which include slab thickness, rod or hole radii and relative unit cell size, provides an immense flexibility in shaping the band structure at any given frequency. We therefore believe that a PC is a viable material platform to realize a practical negative-index lens. Furthermore, by incorporating other optical properties of PCs, highly compact integrated photonic structures can be designed that display a variety of

functionalities such as polarization sensitivity, spatial filtering, routing, and/or imaging. Since our devices are based on Si, there are also abundant opportunities for further integration with electronic devices for preprocessing and postpro-

cessing whenever necessary. In conclusion, we have experimentally demonstrated that the negative index PC is a unique class of materials that can perform as a polarization-sensitive flat lens in large-scale integrated photonic circuits.

---

*Electronic address: won.park@colorado.edu

[1] V. G. Veselago, Sov. Phys. Usp. **10**, 509 (1968).

[2] J. B. Pendry, Contemp. Phys. **45**, 191 (2004).

[3] A. Berrier, M. Mulot, M. Swillo, M. Qiu, L. Thylen, A. Talneau, and S. Anand, Phys. Rev. Lett. **93**, 073902 (2004).

[4] N. Fang, H. Lee, C. Sun, and X. Zhang, Science **308**, 534 (2005).

[5] G. Shvets and Y. A. Urzhumov, Mater. Res. Soc. Symp. Proc. **820**, R1.2.1 (2004).

[6] C. Luo, S. G. Johnson, J. D. Joannopoulos, and J. B. Pendry, Phys. Rev. B **68**, 045115 (2003).

[7] S. Foteinopoulou and C. M. Soukoulis, Phys. Rev. B **67**, 235107 (2003).

[8] D. R. Smith, W. J. Padilla, D. C. Vier, S. C. Nemat-Nasser, and S. Schultz, Phys. Rev. Lett. **84**, 4184 (2000).

[9] Z. Ruan, M. Qiu, S. Xiao, S. He, and L. Thylen, Phys. Rev. B **71**, 045111 (2005).

[10] D. Schurig and D. R. Smith, Phys. Rev. E **70**, 065601(R) (2004).

[11] X. Ao and S. He, Opt. Lett. **30**, 2152 (2005).

[12] M. Notomi, Phys. Rev. B **62**, 10696 (2000).

[13] Z. Ruan and S. He, Opt. Lett. **30**, 2308 (2005).

[14] D. W. Prather, S. Shi, D. M. Pustai, C. Chen, S. Venkataraman, A. Sharkawy, G. J. Schneider, and J. Murakowski, Opt. Lett. **29**, 50 (2004).

[15] R. Zengerle, J. Mod. Opt. **34**, 1589 (1987).

[16] L. Wu, M. Mazilu, and T. F. Krauss, J. Lightwave Technol. **21**, 561 (2003).

[17] E. Schonbrun, M. Tinker, W. Park, and J.-B. Lee, IEEE Photonics Technol. Lett. **17**, 1 (2005).

[18] I. De Leon and F. S. Roux, Phys. Rev. B **71**, 235105 (2005).